IEEE Access
Multidisciplinary | Rapid Review | Open Access Journal

Received March 12, 2019, accepted April 3, 2019, date of publication April 9, 2019, date of current version April 19, 2019.

*Digital Object Identifier 10.1109/ACCESS.2019.2909916*

# A Wind Tunnel Experimental Study on the Flexible Flapping Wing With an Attached Airfoil to the Root

**PENG NIAN[1,2], BIFENG SONG[1], JIANLIN XUAN[3], WENQING YANG[1], AND YUANBO DONG[1]**

[1]Research & Development Institute, Northwestern Polytechnical University, Shenzhen 518057, China
[2]School of Aeronautics, Northwestern Polytechnical University, Xi'an 710072, China
[3]Yangtze River Delta Research Institute, Northwestern Polytechnical University, Taicang 215400, China

Corresponding author: Peng Nian (nian_peng@foxmail.com)

This study was supported by National Key Research and Development Program of China under Grant 2017YFB1300102, National Natural Science Foundation of China under Grant 11872314 and Grant U1613227.

**ABSTRACT** With the purpose to improve the performance of the flexible membrane flapping wing, a kind of flapping wing with an attached airfoil to the root is designed and tested in a wind tunnel. In order to study, the actual performance improvement of the flapping wing, the flight performance is calculated and compared instead of the aerodynamic performance. A method to establish a semi-empirical cycle-averaged mathematical model for the flapping wing with high precision based on the wind tunnel experiment is proposed to calculate the flight performance. The established continuous mathematical model can solve the problem of how to obtain the trimmed state by using discrete experimental data. By attaching the airfoil EPPLER 378 with a thickness of 4.07% chord length to the root, the cruise velocity envelope is expanded, especially with a small cruise velocity. Although the attached airfoil to the root can cause a slight decrease in endurance and range of the flapping wing, it will greatly enhance the climbing performance and effectively reduce the demand for the takeoff sites. Besides, the flapping wing with an attached airfoil to the root will result in a significant reduction in the radius of steady turning and will improve the maneuverability. In addition, the airfoil EJ 85, which is similar to the airfoil EPPLER 378 in shape and camber but has a larger thickness of 6.5% chord length, is attached to the root of the original flapping wing. The same experiment and modeling procedure are performed on the airfoil EJ 85 to analyze the difference in performance of the flapping wing with different airfoil thickness.

**INDEX TERMS** Flapping wing, flight performance, wind tunnel experiment.

## I. INTRODUCTION

Flapping-wing Micro Air Vehicle (FMAV) is a kind of special air vehicle which uses flapping wings to generate both lift and thrust. Many FMAV prototypes have achieved successful flight, e.g. the famous Delfly series [1], [2], MicroBat [3], RoboRaven [4], NanoHummingbird [5], and SmartBird [6] etc. These FMAVs have different flapping wing structures. However, due to the reliability of complex mechanical devices, the FMAV with single-stage flapping wings is the most mature solution adopted by many prototypes which have good flight performance. Nevertheless, compared with the flight of birds, the manmade flapping wing is obviously not an optimal structure. In order to improve the performance of the flapping wing, many researchers have strived to optimize the structure of the flapping wing. Mueller *et al.* [7], Calogero *et al.* [8] developed a passive, one-way folding flapping wing by improving the leading edge structure. It is proved by flight test that this kind of improvements can reduce forward velocity. Kim and Han [9], Li *et al.* [10] developed a smart flapping wing with a macro-fiber composites actuator, in which the camber can be changed by using the surface actuators to enhance the aerodynamic performance. Stewart *et al.* [11] performed a multi-objective optimization method on the shape of a rigid flapping wing to increase the cycle-averaged thrust and reduce the peak of input power. In the case of the AeroVironment NanoHummingbird wing design, the strong coupling problem between flapping deformation and aerodynamic force was approached experimentally [5]. A sample of approximately 300 wings

The associate editor coordinating the review of this manuscript and approving it for publication was Bora Onat.

was designed and tested to find the most efficient flapping wing. These studies indicate that the flapping wing still has potential properties for exploration.

Typically, a flapping wing consists of a carbon fiber skeleton with a curvature and Mylar membrane structure, in order to ensure structural deformation and reduce inertial force. Ultra-thin airfoil usually causes severe airflow separation, which in turn loses aerodynamic force. Dove [12], the FMAV developed in Northwestern Polytechnical University, uses the upper curve of the EPPLER 378 airfoil as the shape of the carbon fiber skeleton. The stall speed is too high due to the fact that the flapping wing adopts the incomplete airfoil, which seriously affects the landing stability.

In order to improve the aerodynamic performance of the flexible membrane flapping wing and solve its problem of easily stalling, the paper designed a flexible single-stage flapping wing with an attached airfoil near to the root, inspired by the thickness distribution of birds' wings and the relationship between airfoil thickness and stall speed. And studied the effect of the improvement on the flapping wing performance through wind tunnel experiments.

Usually, the performance evaluation of the flapping wing is simply to compare the aerodynamic force [13] or propulsion efficiency [14] in the same state. But since the lift and thrust cannot be generated separately for the flapping wing, these methods cannot evaluate the performance of the flapping wing in actual flight conditions. Therefore, we propose to use the flight performance parameters to evaluate the performance. In order to solve the difficulty of the calculation of flight performance parameters caused by the discontinuity of the experimental state, the paper also proposes a semi-empirical cycle-averaged mathematical model for the flapping wing based on wind tunnel experimental data.

## II. EXPERIMENT SETUP

The tested flapping wing structure was designed and fabricated. According to the performance of the experimental system, the wind tunnel experimental state is selected reasonably. After that data acquisition and postprocessing are performed.

### A. FLAPPING WING MODEL

In order to study the effect of attaching an airfoil with certain thickness near to the flapping root on the performance, a flapping wing structure is designed on the basis of Dove, which has a semi-span of 0.3 meters and a root chord length of 0.1 meter. A lightweight foam structural component is attached between the first chord and the third chord. The structural component is 0.1 meter long and its width is the same as the flapping wing root chord. The specific position of the structural component on the flapping wing is shown in Fig. 1. The characteristics of this structure are as following:

a. The attached structural component is located in the triangular region of the flapping wing skeleton, and from previous research [12], the region is less deformed during the flapping. That is, the attached structural component has less influence on the deformation of the overall structure of the flapping wing;
b. Attaching an airfoil structural component near the root of the flapping wing can reduce the effects of inertial forces caused by the attached mass;
c. The inner part of the flapping wing is mainly related to the lift, and the tangential speed of this part is small, and thus the aerodynamic mechanism is similar to that of the fixed wing, which helps to enhance the effect of the attached airfoil.

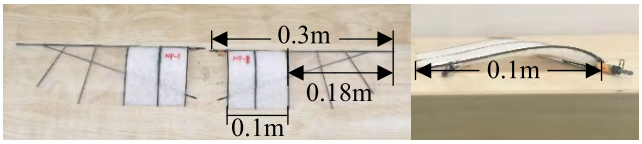


**FIGURE 1.** Flexible flapping wing with the EPPLER 378 airfoil attached to the root.

**TABLE 1.** The mass of the experimental flapping wing.

| Flapping wing | Mass (g) |
|---|---|
| Dove's original flapping wing (hereinafter referred to as FW10) | 12.0 |
| Attaching the complete EPPLER 378 airfoil to Dove's flapping wing (hereinafter referred to as FW378) | 14.7 |

The mass of the experimental flapping wing is shown in Table I. Due to the lightweight foam structure, the added mass is smaller, and so it merely has a slight influence on the input power.

### B. WIND TUNNEL AND EXPERIMENTAL PROCEDURE

The experiment is carried out by using the FMAV wind tunnel experimental measurement and a control system developed by our research group. The system can adjust the flapping frequency with high precision by controlling the rotation speed of a servo motor. The measurement system can collect experimental variables such as flapping angular displacement, six-axis forces/moments and input power in real time at a sampling rate of 2000Hz.

The ATI Nano 17 multi-axis load cell is chosen as a balance. The load cell has the advantages of small size, high precision and fast response, which is suitable for wind tunnel experiments of flapping wings. There are several flapping amplitudes can be chosen for the flapping mechanism shown in Fig. 2, and the flapping amplitude of 61° is selected because it is close to the Dove.

The experiment is carried out in the low-speed aeroacoustic wind tunnel of Northwestern Polytechnical University. The wind tunnel is an open jet return flow type. The test section has a diameter of 1.5m and a length of 1.9m. The average turbulence is 0.2% and the test wind speed is 6–40m/s. Its parameters are suitable for the full-scale model experiment of the flapping wing. The installed model in the wind tunnel is shown in Fig. 3.

Based on the performance of the experimental system and our research purposes, the experimental conditions are

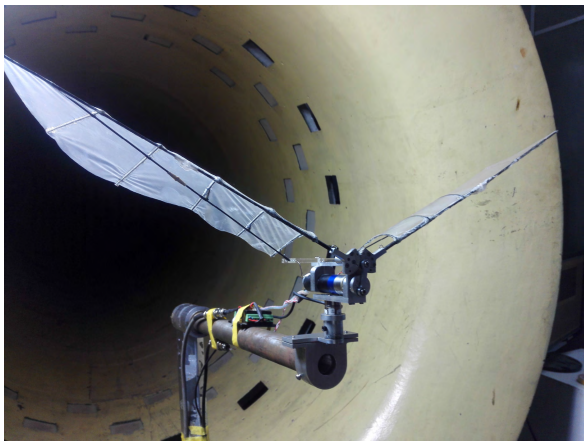

**FIGURE 2.** Experimental device with FW10 installed.

**FIGURE 3.** Installation of the experimental system in the wind tunnel.

**TABLE 2.** Experimental states.

| Experimental variable | Value |
|---|---|
| *V (m/s)* | 8,10,12 |
| *f (Hz)* | 4,5,6 |
| *α (degree)* | 0,3,6,9,12,15 |

In all experiments, the initial value of the data is cleared at the beginning with the state of $\alpha = 0$ and $V = 0$.

selected as shown in Table II. Experiments are carried out to collect data such as aerodynamic force, flapping angular displacement and input power in the corresponding states of the two kinds of flapping wings.

In order to eliminate the aerodynamic interference and the gravity interference of the experimental device in the collected experimental data, and also to acquire the drag of the flapping wing in the non-flapping state, the following experimental states are added:

a. State 1: in the condition that the flapping wing is not installed, the forces and moments at all angles of attack in Table II are measured;
b. State 2: in the condition that the flapping wing is not installed, the forces and moments at all speeds and angles of attack in Table II are measured;
c. State 3: the experimental flapping wing is installed, and the forces and moments at all angles of attack in Table II are measured;
d. State 4: the experimental flapping wing is installed, and fixed in the horizontal state, and the forces and moments at all speeds and angles of attack in Table II are measured.

### C. DATA ACQUISITION AND POSTPROCESSING

#### 1) AERODYNAMIC INTERFERENCE

The aerodynamic force generated by the experimental device installed on the balance during the experiment is the interference that needs to be removed. The aerodynamic interference data measured in state 2 also includes the gravity interference of the experimental device. Therefore, it is necessary to calculate the weight of the experimental device $G_{mec}$ and the vertical distance between its center of gravity and the center of the balance $l_{mec}$. The decomposition of the flapping mechanism weight $G_{mec}$ in the load cell coordinate system can be expressed as the following.

$$\left.\begin{aligned} F_{x.1} &= -G_{mec}\sin\alpha \\ T_{y.1} &= F_{x.1}l_{mec} = -G_{mec}l_{mec}\sin\alpha \end{aligned}\right\} \tag{1}$$

where $F_{x.1}$ and $T_{y.1}$ are the x-axis force and the y-axis moment of the balance coordinate system measured in state 1 respectively. In this way, $G_{mec}$ and $l_{mec}$ are solved by Eq. (1). The values of $G_{mec}$ and $l_{mec}$ obtained at different angles of attack are averaged to ensure the consistency of the calculated gravity component.

In this paper, we only study the longitudinal characteristics of the flapping wing in the condition of non-sideslip flight. Therefore, we only need to obtain the aerodynamic interference of the experimental devices in the x-axis force component, the z-axis force component and the y-axis moment component. The aerodynamic interference ($F_{x.2}$, $F_{z.2}$, $T_{y.2}$) measured in experimental state 2 includes the gravity interference ($G_{mec.x}$, $G_{mec.z}$, $T_{mec.y}$) of the flapping mechanism. The pure aerodynamic interference ($F_{x.aero}$, $F_{z.aero}$, $T_{y.aero}$) are obtained by subtracting the gravity interference from the data measured in experimental state 2. The gravity interference is represented by decomposing the gravity of the experimental device in the load cell coordinate system.

$$\left.\begin{aligned} F_{x.aero} &= F_{x.2} - G_{mec.x} \\ F_{z.aero} &= F_{z.2} - G_{mec.z} \\ T_{y.aero} &= T_{y.2} - T_{mec.y} \\ G_{mec.x} &= -G_{mec}\sin\alpha \\ G_{mec.z} &= -G_{mec}\cos\alpha + G_{mec} \\ T_{mec.y} &= -G_{mec}l_{mec}\sin\alpha \end{aligned}\right\} \tag{2}$$

#### 2) GRAVITY INTERFERENCE

In addition to the aerodynamic interference of the experimental device, the gravity interference of the experimental device with the flapping wing at different angles of attack also has a strong influence on the experimental results. Using the data obtained in state 3, the weight of the experimental device with the flapping wing $G_{mw}$ and the vertical distance between the center of gravity and the center of the balance $l_{mw}$ are calculated according to Eq. (3). The values obtained at different angles of attack are averaged to ensure the consistency of calculations.

$$\left.\begin{aligned} F_{x.3} &= -G_{mw}\sin\alpha \\ T_{y.3} &= F_{x.3}l_{mw} = -G_{mw}l_{mw}\sin\alpha \end{aligned}\right\} \tag{3}$$

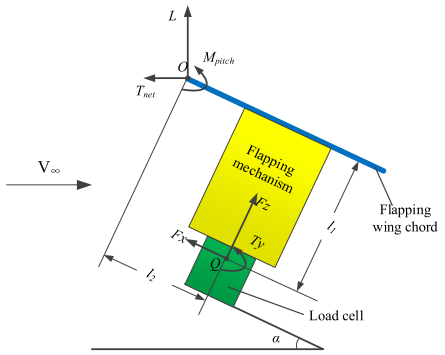


**FIGURE 4.** Experimental device coordinate system definition diagram.

After obtaining the experimental interferences, the experimental data is acquired according to all the states in Table II (recorded as state 5). The aerodynamic interference and the gravity interference of the experimental device are subtracted in Eq. (4) to obtain the actual aerodynamic data of the experimental flapping wing $(F_x, F_z, T_y)^T$.

$$\left.\begin{aligned} F_x &= F_{x.5} - F_{x.aero} - G_{mw.x} \\ F_z &= F_{z.5} - F_{z.aero} - G_{mw.z} \\ T_y &= T_{y.5} - T_{y.aero} - T_{mw.y} \\ G_{mw.x} &= -G_{mw} \sin\alpha \\ G_{mw.z} &= -G_{mw} \cos\alpha + G_{mw} \\ T_{mw.y} &= -G_{mw} l_{mw} \sin\alpha \end{aligned}\right\} \tag{4}$$

### 3) AXIS TRANSFORMATION

In the experiment, the force and moment are acquired in the balance coordinate system. Therefore, it is necessary to convert them into the wind axis coordinate system for analysis. And the reference point of the longitudinal moment needs to be transferred from the center of the balance to the leading edge of the flapping wing for comparison. Fig. 4 is a schematic diagram of the definitions of the coordinates of the experimental device [15]. The distance between the center of the balance and the flapping wing chord is $l_1$, and $l_2$ is the horizontal distance between the center of the balance and the leading edge of the flapping wing. $L$, $T_{net}$ and $M_{pitch}$ are the lift, net thrust and pitch moment of the flapping wing respectively.

The experiment focuses on the effect of the improved flapping wing on the actual flight, and so there is no need to remove the inertial force component of the flapping wing. $(F_x, F_z, T_y)$ are separately decomposed and integrated in the wind axes system to obtain the conversion Eq. (5), in which pre-measured $l_1$ and $l_2$ are used in the transfer process, as defined in Fig. 4.

$$\begin{bmatrix} L \\ T_{net} \\ M_{pitch} \end{bmatrix} = \begin{bmatrix} \sin\alpha & \cos\alpha & 0 \\ \cos\alpha & -\sin\alpha & 0 \\ -l_1 & l_2 & 1 \end{bmatrix} \begin{bmatrix} F_x \\ F_z \\ T_y \end{bmatrix} \tag{5}$$

In this chapter, the wind tunnel experimental data of FW10 and FW378 are acquired and the experimental interference is removed by postprocessing. The post-processed data can be used in the following modeling process.

## III. FLAPPING WING MODELING BASED ON WIND TUNNEL EXPERIMENT

The aerodynamic forces of the flexible flapping wing have a strong coupling relationship with the structural deformation. Therefore, the wind tunnel experiment is usually conducted to obtain more accurate aerodynamic data. However, the state of the wind tunnel experiment is usually discrete and its interval cannot be too small considering the high cost of the experiment, which makes it difficult to obtain the trim state in the performance calculation. Therefore, due to the discreteness, the analysis of the aerodynamic characteristics of the flapping wing is usually performed by solving the set that satisfies the state of the trim condition [16]. In order to improve the accuracy of the solution, the paper proposes a semi-empirical flapping wing modeling method based on the experimental data characteristics and the mechanism of aerodynamic forces and power production.

### A. CYCLE-AVERAGED LIFT MODELING METHOD

According to the relationship between the cycle-averaged lift and the angle of attack in the experimental data, it can be seen that the former is similar to the case of the fixed wing, which is linear with the angle of attack before stall. Therefore, the cycle-averaged lift can be expressed in the form in Eq. (6). In addition, the wind speed and the flapping frequency also have effects on the cycle-averaged lift, but the relationship is complicated due to the special fluid-solid coupling characteristics of the flapping wing. To simplify the calculation, these effects are reflected in the polynomial form of $L_\alpha$ and $L_0$.

$$\left.\begin{aligned} \overline{L} &= \overline{L_\alpha}\alpha + \overline{L_0} \\ \overline{L_\alpha} &= F(V, f) \\ \overline{L_0} &= F(V, f) \end{aligned}\right\} \tag{6}$$

where the defined slope of lift line $L_\alpha$ is a function of flight speed and flapping frequency. $L_0$ is the lift when the angle of attack is zero.

### B. CYCLE-AVERAGED NET THRUST MODELING METHOD

The cycle-averaged net thrust $T_{net}$ is also related to three variables, but the situation is more complicated. Considering that the net thrust of the flapping wing contains both drag and thrust components, it is usually difficult to completely separate the thrust from the drag. The thrust characteristics of the flapping wing can be considered to be similar to the propeller [17]. Therefore, the net thrust of the flapping wing is approximately divided into the thrust generated by the flapping and the constant drag $D$ unrelated to it. Referring to the thrust calculation formula of the propeller, the thrust is expressed as the square of the flapping frequency multiplied by the coefficient $T_f$. This form of thrust contains the additional drag change caused by the flapping motion. The cycle-averaged net thrust of the flapping wing can be expressed as

Eq. (7).

$$\left.\begin{aligned} \overline{T_{net}} &= \overline{T_{flap}} - D \\ \overline{T_{flap}} &= \overline{T_f} f^2 \\ \overline{T_f} &= F(V, \alpha) \\ D &= F(V, \alpha) \end{aligned}\right\} \tag{7}$$

where $T_f$ is a fitting polynomial that includes the effects of the wind speed and the angle of attack on the thrust. $D$ is fitted to this polynomial by experimental data.

### C. CYCLE-AVERAGED INPUT POWER MODELING METHOD

The input power of the flapping wing $P_{in}$ is mainly related to the torque and the flapping angular speed attached to the flapping shaft. According to the rotational power calculation formula, the input power of the flapping wing can be expressed as the torque attached to the flapping shaft multiplied by the flapping angular velocity. So the cycle-averaged input power can be expressed as Eq. (8).

$$\left.\begin{aligned} \overline{P_{in}} &= \overline{M_{wing}\omega} \\ \overline{M_{wing}} &= (L\cos\alpha - T_{net}\sin\alpha) l_{cp.y}/\eta = F(V, f) \\ \overline{\omega} &= F(A, f) \end{aligned}\right\} \tag{8}$$

Among them, $M_{wing}$ represents the flapping shaft torque; $\omega$ is the flapping angular velocity; and $\eta$ is the transmission efficiency of the experimental device. The flapping angular velocity is related to the flapping amplitude $A$ and the flapping frequency $f$. Under a certain flapping amplitude, the cycle-averaged angular velocity is a function of the flapping frequency. The instantaneous aerodynamic force in the expression of the cycle-averaged flapping shaft torque is independent of the angle of attack approximately, according to experimental data (the angle of attack does not change the amplitude of instantaneous aerodynamic forces). The spanwise center of pressure $l_{cp.y}$ has a relatively fixed position. The transmission efficiency of the experimental device is related to the flapping frequency. Based on the above factors, the cycle-averaged flapping shaft torque can be simplified as a fitting polynomial form of the wind speed and frequency.

### D. MODELING RESULTS

According to the above flapping wing modeling method, the corresponding parameters are fitted using the least-square fitting method, based on wind tunnel experimental data. FW10 and FW378 are modeled respectively based on the method mentioned in Chapter III using the experimental data after postprocessing. The modeling results of FW10 and FW378 are shown in Eq. (9) to (11) and Eq. (12) to (14) respectively. The model accuracy is shown in Tables III and IV.

$$\left.\begin{aligned} \overline{L} &= \overline{L_0} + \overline{L_\alpha}\alpha \\ \overline{L_\alpha} &= 4.39 - 0.0152f - 0.6453V \\ &\quad + 0.004652fV + 0.07431V^2 \\ \overline{L_0} &= -0.4664 + 0.01119f + 0.108V \\ &\quad + 0.001459fV - 0.006571V^2 \end{aligned}\right\} \tag{9}$$

**TABLE 3.** FW10 modeling results.

| Object | RMSE | $R^2$ |
|---|---|---|
| $\overline{L}$ | 0.0303 | 0.9959 |
| $\overline{T_{net}}$ | 0.0244 | 0.9876 |
| $\overline{P_{in}}$ | 0.5811 | 0.9459 |

**TABLE 4.** FW378 modeling results.

| Object | RMSE | $R^2$ |
|---|---|---|
| $\overline{L}$ | 0.0230 | 0.9983 |
| $\overline{T_{net}}$ | 0.0111 | 0.9964 |
| $\overline{P_{in}}$ | 0.2407 | 0.9770 |

$$\left.\begin{aligned} \overline{T_{net}} &= \overline{T_f} f^2 - D \\ \overline{T_f} &= -0.003155 + 0.005332\alpha \\ &\quad + 0.002319V + 0.1916\alpha^2 \\ &\quad - 0.006886\alpha V - 0.0001403V^2 \\ &\quad - 0.1397\alpha^3 - 0.01747\alpha^2 V \\ &\quad + 0.0007434\alpha V^2 \\ D &= -1.685 + 1.235\alpha + 0.3758V \\ &\quad - 1.571\alpha^2 - 0.1604\alpha V \\ &\quad - 0.02294V^2 \end{aligned}\right\} \tag{10}$$

$$\left.\begin{aligned} \overline{P_{in}} &= \overline{M_{wing}\omega} \\ \overline{M_{wing}} &= 1.862 - 0.103f - 0.1114V \\ &\quad + 0.009929f^2 - 0.005195fV \\ &\quad + 0.007971V^2 \\ \overline{\omega} &= 1.993f(-0.01591f + 1.255) \end{aligned}\right\} \tag{11}$$

$$\left.\begin{aligned} \overline{L} &= \overline{L_0} + \overline{L_\alpha}\alpha \\ \overline{L_\alpha} &= -1.49 + 0.1238f + 0.3946V \\ &\quad - 0.006687fV + 0.03239V^2 \\ \overline{L_0} &= -0.5494 - 0.02597f + 0.1498V \\ &\quad + 0.005114fV - 0.00725V^2 \end{aligned}\right\} \tag{12}$$

$$\left.\begin{aligned} \overline{T_{net}} &= \overline{T_f} f^2 - D \\ \overline{T_f} &= -0.01036 + 0.0216\alpha \\ &\quad + 0.003888V + 0.155\alpha^2 \\ &\quad - 0.00835\alpha V - 0.0002081V^2 \\ &\quad - 0.2718\alpha^3 - 0.007094\alpha^2 V \\ &\quad + 0.0006177\alpha V^2 \\ D &= -1.537 + 1.436\alpha + 0.3368V \\ &\quad - 2.188\alpha^2 - 0.164\alpha V \\ &\quad - 0.0206V^2 \end{aligned}\right\} \tag{13}$$

$$\left.\begin{aligned} \overline{P_{in}} &= \overline{M_{wing}\omega} \\ \overline{M_{wing}} &= 1.555 - 0.3234f + 0.1306V \\ &\quad + 0.02213f^2 + 0.0032fV \\ &\quad - 0.007304V^2 \\ \overline{\omega} &= 1.99f(-0.01379f + 1.255) \end{aligned}\right\} \tag{14}$$

The RMSE in Tables III and IV indicates the root mean squared error. The smaller the RMSE is, the smaller the error between the model and the modeling data is. $R^2$ represents the coefficient of determination. The closer $R^2$ is to "1", the better the model fits the data.

The modeling results show that the accurate flapping wing aerodynamic model and input power model can be established by using the modeling method proposed in the paper. At the same time, since the established models are based on polynomials, it is feasible to perform extrapolation in the linear range, which can supplement the deficiency of the experimental state. The analysis below is conducted based on the established flapping wing model.

## IV. PERFORMANCE CALCULATION

Generally, the performance improvement of the flapping wing is only compared by lift and thrust. However, the comparison of the aerodynamic forces alone can not reflect the impact of the improvement on the actual flight performance of the FMAV. Therefore, we propose to evaluate the improvement of the flapping wing by flight performance.

The flapping wing is characterized by significant cyclical aerodynamic effects, which makes it difficult to calculate its performance. Sun *et al*. [18] considered that when the mass of the flapping wing was neglected, the flapping wing dynamics equation could be simplified to the fixed-wing aircraft dynamics equation. In the actual test flight, Dove still has the aerodynamic characteristics similar to the fixed wing. Therefore, the flapping wing aerodynamics can be cycle-averaged and then analyzed with reference to the performance calculation method of the fixed wing. In this paper, we summarize four aspects that are suitable to describe the performance of the flapping wing

The scalar form of the fixed-wing kinetic equation of the center of mass in the navigational coordinate system is as follows [19]:

$$\left.\begin{aligned} m\tfrac{dV}{dt} &= T\cos\alpha\cos\beta - D - mg\sin\gamma \\ mV\cos\gamma\tfrac{d\chi}{dt} &= T[\sin\alpha\sin\mu - \cos\alpha\sin\beta\cos\mu] \\ &\quad + C\cos\mu + L\sin\mu \\ -mV\tfrac{d\gamma}{dt} &= T[-\sin\alpha\cos\mu - \cos\alpha\sin\beta\sin\mu] \\ &\quad + C\sin\mu - L\cos\mu + mg\cos\gamma \end{aligned}\right\} \quad (15)$$

where for the flapping wing, since thrust cannot be generated independently of lift, and thrust and drag are difficult to separate, only net thrust can be directly obtained [20]. So the body axes system thrust in Eq. (15) is decomposed into the wind axes system and Eq. (16) introduces the cycle-averaged net thrust and the cycle-averaged lift into Eq. (15).

$$\left.\begin{aligned} \overline{T_{net}} &= T\cos\alpha - D \\ \overline{L} &= L + T\sin\alpha \end{aligned}\right\} \quad (16)$$

For a flapping wing, the cycle-averaged lift and net thrust are just a function of three parameters, after given the amplitude of the flapping [21]:

$$\left.\begin{aligned} \overline{T_{net}} &= F(V, f, \alpha) \\ \overline{L_{net}} &= F(V, f, \alpha) \end{aligned}\right\} \quad (17)$$

### A. STEADY LEVEL FLIGHT PERFORMANCE CALCULATION

When a FMAV is in steady level flight, there are velocity variation rate $dV/dt = 0$, flight path angle variation $d\gamma/dt = \gamma = 0$, heading angle variation rate $d\chi/dt = 0$, angle of sideslip $\beta = 0$, speed roll angle $\mu = 0$ and lateral force $C = 0$. Bring these conditions and Eq. (16) into Eq. (15) to obtain the level flight equilibrium equation shown in (18).

$$\left.\begin{aligned} \overline{T_{net}} &= 0 \\ \overline{L_{net}} &= W \end{aligned}\right\} \quad (18)$$

That is, the cycle-averaged net thrust of the flapping wing is zero; the cycle-averaged lift is equal to the gravity of the FMAV $W$; and the FMAV is in equilibrium. Given a $V$, Eq. (18) contains only two unknown variables $f$ and $\alpha$. The equations are close and the angle of attack and the flapping frequency at the given flight speed can be solved. The trimmed state is solved at a certain speed interval within a reasonable speed range, until a speed boundary that cannot be trimmed is obtained. At this time, the minimum level flight speed and the maximum one of the flapping wing can be obtained. Usually the maximum flapping frequency determines the maximum trim speed and the stall angle of attack limits the minimum trim speed. The faster the maximum flight speed, the stronger the front wind resistance, and the slower the minimum flight speed, the more favorable the stability of the landing phase.

### B. POWER CONSUMPTION PERFORMANCE CALCULATION

The power consumption performance of a flapping wing includes endurance and range. In order to calculate the maximum endurance and range of a FMAV, it is necessary to determine the speed for the maximum endurance $V_{E.max}$ and the speed for the maximum range $V_{R.max}$. FMAVs generally use a lithium-polymer battery as the energy supply device. The weight of the FMAV remains unchanged during the flight, so the speed for the maximum endurance is the minimum power speed that satisfies the steady level flight condition. The speed for the maximum range is the corresponding state to the minimum power per unit distance. Using the graphic method, a straight line that starts at the origin is tangent to the trim speed vs power curve of the steady level flight. The speed corresponding to the tangent point is the maximum range speed.

When the maximum endurance speed and the maximum range speed are obtained, the maximum endurance and range can be expressed as:

$$E_{\max} = \frac{W_{batt}}{P_{\min}} \quad (19)$$

$$R_{\max} = \frac{3.6W_{batt}}{P_{V_{R.\max}}} V_{R.\max} \quad (20)$$

wherein $W_{batt}$ is the energy of the battery; $P_{VR.max}$ is the power corresponding to the speed of the maximum range. In Eq. (19) and (20), the influence of the effective capacity of the battery with the change of the discharge power on endurance is neglected. And the influence of the wind on the ground speed is neglected when calculating the range.

### C. STEADY CLIMBING AND DESCENDING FLIGHT PERFORMANCE CALCULATION

In the state of a steady climbing and descending flight, there are $dV/dt = 0$, $d\gamma/dt = 0$, $d\chi/dt = 0$, $\beta = 0$, $\mu = 0$, and $C = 0$. Bring these conditions and Eq. (16) into Eq. (15) to obtain the steady climbing and descending flight equilibrium equation shown in (21).

$$\left.\begin{aligned} \overline{T_{net}} &= W \sin\gamma \\ \overline{L} &= W \cos\gamma \end{aligned}\right\} \tag{21}$$

The flight path angle $\gamma$ can be obtained from Eq. (21):

$$\left.\begin{aligned} \tan\gamma &= \frac{\overline{T_{net}}}{\overline{L}} \\ \gamma &= \arctan\left(\frac{\overline{T_{net}}}{\overline{L}}\right) \end{aligned}\right\} \tag{22}$$

The height is defined as $H$, and the cycle-averaged net thrust equation in Eq. (21) is introduced into Eq. (23) to obtain the equation of the vertical velocity $V_v$.

$$V_v = \frac{dH}{dt} = V\sin\gamma = \frac{\overline{T_{net}}V}{W} \tag{23}$$

In order to minimize the horizontal distance $R_c$ through which the FMAV climbs to the safe altitude $H_{safe}$ and reduce the demand for the take-off site, the flight path angle should be maximized. The minimum $R_c$ is:

$$R_{\mathrm{c.min}} = H_{safe}\cot\gamma_{\max} \tag{24}$$

To reach the safe height rapidly, specific excess power ($T_{net}V$) should be taken to the maximum. In this state, the maximum climb rate is obtained. The minimum climb time $t_{c.min}$ can be expressed as:

$$t_{c.\min} = \frac{H_{safe}}{V_{v.\max}} \tag{25}$$

### D. STEADY TURNING FLIGHT PERFORMANCE CALCULATION

In the state of steady turning flight, there are $dV/dt = 0$, $d\gamma/dt = \gamma = 0$, $\beta = 0$, and $C \approx 0$. Bring these conditions and Eq. (16) into Eq. (15) to obtain the steady turning flight equilibrium equation shown in (26).

$$\left.\begin{aligned} \overline{T_{net}} &= 0 \\ mV\frac{d\chi}{dt} &= \frac{W}{g}\frac{V^2}{r} = \overline{L}\sin\mu \\ \overline{L}\cos\mu &= W \end{aligned}\right\} \tag{26}$$

wherein, $g$ is the acceleration of gravity, and $r$ is the radius of turning flight. The minimum turning radius can be obtained by Eq. (26) [19].

$$r_{\min} = \frac{1}{g}\left(\frac{V^2}{\tan\mu}\right)_{\min} = \frac{1}{g}\left(\frac{V^2}{\sqrt{n_n^2 - 1}}\right)_{\min} \tag{27}$$

A small turning radius means that the FMAV has better maneuverability, which can significantly expand its usage scenarios. The turning radius can be decreased by reducing the flight speed and increasing the speed roll angle, but the minimum flight speed and the maximum speed roll angle have certain limits. When the speed reduces, the angle of attack must increase to maintain gravity balance, while the maximum angle of attack needs to be limited to the stall angle of attack. The maximum speed roll angle is limited by the FMAV maximum overload.

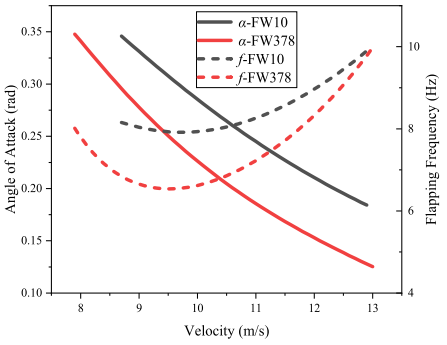


**FIGURE 5.** FW10 and FW378 steady level flight performance calculation results.

This chapter provides the calculation process and calculation method of the flight performance of the flapping wing with reference to the calculation method of the fixed wing flight performance. Combined with the flapping wing mathematical model established in Chapter III, the actual flight performance of the flapping wing can be compared and analyzed.

## V. PERFORMANCE COMPARISON BETWEEN ORIGINAL FLAPPING WING AND FLEXIBLE FLAPPING WING WITH AN ATTACHED EPPLER 378 AIRFOIL TO THE ROOT

Based on the data of Dove, given the takeoff weight $W_{to} =$ 180g, the limit of the maximum angle of attack is set to 20 degrees and the maximum flapping frequency is 10 Hz. Based on the flapping wing model established in Chapter 3, the performance calculation methods in Chapter 4 are used to calculate and compare the different performances of the two experimental flapping wings.

### A. STEADY LEVEL FLIGHT PERFORMANCE COMPARISON

The flapping frequency and the angle of attack that satisfy Eq. (18) are solved at different flight speeds, the result is shown in Fig. 5. According to the calculation result, the trimmed angle of attack gradually decreases with the trimmed velocity, which shares similar characteristics with the fixed wing. Compared with the original flapping wing FW10, the flapping wing FW378 with the complete EPPLER 378 airfoil attached to the root has a significantly lower minimum trimmed velocity, which will help to improve the stability of the FMAV during the landing phase. The two flapping wings almost have the same maximum trimmed velocity since it is mainly related to the flapping frequency. In addition, FW378 has a smaller trimmed angle of attack and flapping frequency than FW10, which indicates that the aerodynamic performance of FW378 has been greatly improved.

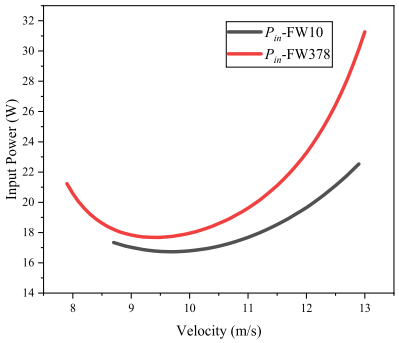


**FIGURE 6.** FW10 and FW378 power consumption performance calculation results.

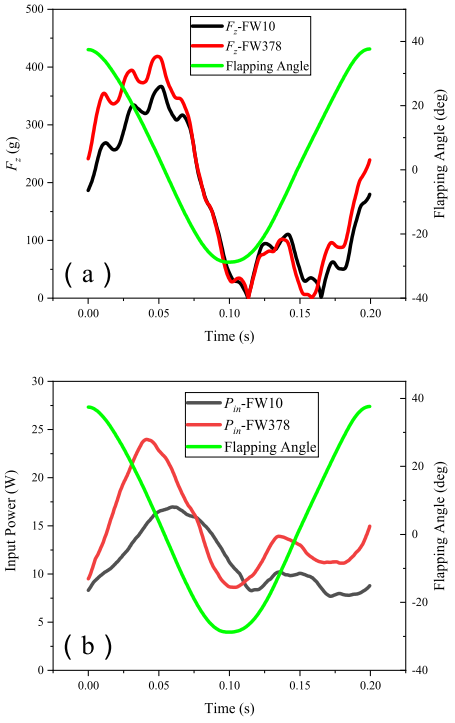


**FIGURE 7.** FW10 and FW378 instantaneous experimental data comparison (at $V = 10$m/s, $f = 5$Hz, $\alpha = 12°$ ). (a) The absolute value of the z-axis force component of the load cell. (b) Experimental servo motor instantaneous input power.

### B. POWER CONSUMPTION PERFORMANCE COMPARISON

According to the steady level flight trimmed state calculated in Section A, the established flapping wing power model is used to calculate the input power of the corresponding state. The curve of the trimmed velocity and the input power is shown in Fig. 6. The calculation result shows that the input power of FW378 is higher than that of FW10 in the entire trimmed velocity envelope.

Fig. 7 is the experimental data of the absolute values of instantaneous $F_z$ and $P_{in}$ in a cycle. FW378 has a larger aerodynamic force on the vertical flapping wing surface $F_z$ in the first half stage of the down stroke, and $F_z$ is increased due to the suppression of airflow separation in the latter stage of the up stroke. The increase in $F_z$ indirectly causes the flapping shaft torque to be greater than that of FW10, which is directly related to the input power, thus resulting in an increase in the cycle-averaged input power.

**TABLE 5.** The maximum endurance and maximum range comparison.

| Flapping wing | $V_{E.max}$ (m/s) | $E_{max}$ (h) | $V_{R.max}$ (m/s) | $R_{max}$ (km) |
|---|---|---|---|---|
| FW10 | 9.7 | 0.72 | 11.2 | 27.35 |
| FW378 | 9.4 | 0.69 | 10.6 | 25.01 |

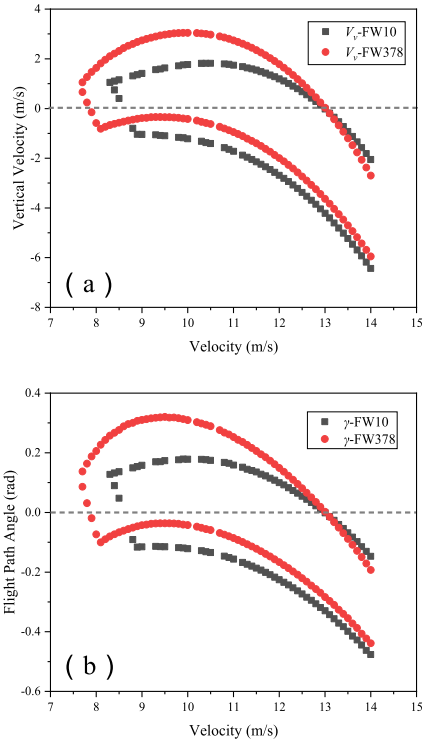


**FIGURE 8.** FW10 and FW378 steady climbing and descending trimmed state boundary. (a) Trimmed vertical velocity boundary. (b) Trimmed flight path angle boundary.

The maximum endurance speed $V_{E.max}$ and the maximum range speed $V_{R.max}$ of the two experimental flapping wings are determined by a graphic method. Assume the capacity of a battery is 15.4Wh and the power of airborne equipment is 5W, ignoring the Peukert effect. The maximum endurance $E_{max}$ and the maximum range $R_{max}$ of the two experimental flapping wings calculated according to Eq. (19) and (20) are shown in Table V. The endurance and range of FW378 will have a certain loss.

### C. STEADY CLIMBING AND DESCENDING FLIGHT PERFORMANCE COMPARISON

Since Eq. (21) is not close the method of traversing in the state domain is used to calculate the steady climbing and descending flight performance. There are many trimmed points at each speed, which form a trimmed area. For the convenience of comparison, the boundary state of the trimmed area is extracted, and the flight path angle and the vertical speed in the corresponding state are calculated by Eq. (22) and

**TABLE 6. The extreme horizontal distance of take off and land comparison.**

| Flapping wing | Climb $\gamma_{max}$ (rad) | Take off $R_{c.min}$ (m) | Descend $\gamma_{max}$ (rad) | Land $R_{c.min}$ (m) |
|---|---|---|---|---|
| FW10 | 0.18 | 82.68 | -0.12 | 128.29 |
| FW378 | 0.32 | 45.26 | -0.10 | 148.84 |

The maximum descend angle is obtained at the lowest trimmed velocity.

**TABLE 7. The minimum turning radius comparison.**

| Flapping wing | $r_{min}$ (m) |
|---|---|
| FW10 | 12.88 |
| FW378 | 8.78 |

Eq. (23) respectively. The steady climbing and descending trimmed state boundary is shown in Fig. 8.

It can be seen from Fig. 8 that FW378 has a larger climbing vertical velocity and angle of climb than FW10. In terms of descending performance, the difference between the two flapping wings at a high speed is not obvious. FW378 can descend at a lower speed and maintain a similar vertical velocity than FW10. Therefore, FW378 is easier to control when landing, and the remaining energy is small which is beneficial to reduce the impact on the fuselage when landing. The safety height $H_{safe}$ is set as 15m and the limit takeoff and land horizontal distance of the two experimental flapping wings are calculated according to Eq. (24), the results of which are shown in Table VI. According to the calculation results, the horizontal distance climbing to the safe height is significantly shortened after attaching the complete EPPLER 378 airfoil to the root, which is beneficial to reduce the requirement for takeoff site. Meanwhile, the horizontal distance of landing of the two flapping wings is not much different.

### D. STEADY TURNING FLIGHT PERFORMANCE COMPARISON

Since Eq. (26) is also not close, the traversal calculation is also performed in the state domain to find the states that satisfy the condition of the steady turning. The turning radius in the corresponding state is calculated by Eq. (27) according to the obtained trimmed state. The steady turning flight trimmed state form an area. Fig. 9 is the outermost boundary of the steady turning flight trimmed state. The minimum turning radiuses of FW10 and FW378 are shown in Table VII. The normal overload $n_n$ of FW378 over the entire trimmed velocity range is significantly greater than that of FW10, indicating that FW378 is capable of producing greater lift, which results in a smaller turning radius. The smaller turning radius helps to improve the maneuverability of the FMAV to adapt to a narrow flight environment.

By comparing the flight performance of FW10 and FW378, it can be seen that attaching an airfoil to the root can greatly improve the level flight, climb flight and turning flight performance. At the same time, it has a slight adverse effect on endurance.

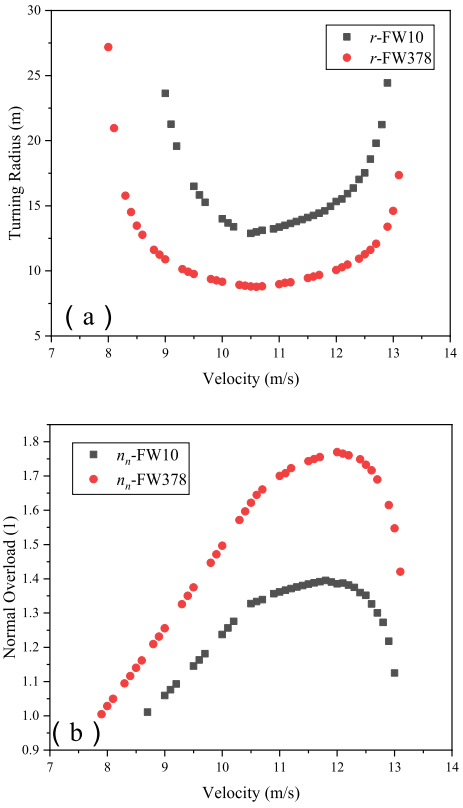


**FIGURE 9. FW10 and FW378 steady turning trimmed state boundaries. (a) Trimmed turning radius boundary. (b) Trimmed normal overload boundary.**

**TABLE 8. Comparison of geometric parameters between eppler 378 airfoil and ej 85 airfoil.**

| Airfoil | Profile | Geometric Parameter |
|---|---|---|
| EPPLER 378 |  | Maximum thickness: 4.07%$c$<br>Maximum camber:7.99%$c$ |
| EJ 85 |  | Maximum thickness: 6.50%$c$<br>Maximum camber:8.50%$c$ |

$c$ indicates the chord length of the airfoil.

## VI. PERFORMANCE COMPARISON BETWEEN FLEXIBLE FLAPPING WING WITH AN ATTACHED EPPLER 378 AIRFOIL AND EJ 85 AIRFOIL TO THE ROOT

From the analysis and calculation in Chapter V, it can be seen that the addition of the airfoil with certain thickness to the wing root has a positive effect on the aerodynamic force of the flapping wing. In order to study the influence of airfoil with different thickness attached to the root, the paper selects the EJ 85 airfoil which has a similar camber but greater thickness than the EPPLER 378 airfoil. The specific parameters of the airfoil are shown in Table VIII. The structure of the experimental flapping wing with EJ 85 airfoil attached to Dove's flapping wing root (hereinafter referred to as FW85) is identical to that of FW378, as shown in Fig. 10. The FW85 has a mass of 15.3g.

The data acquisition of the wind tunnel experimental states in Table II are also carried out for FW85. The mathematical

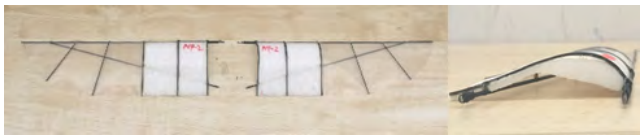

**FIGURE 10.** Flexible flapping wing with EJ 85 airfoil attached to the root.

**TABLE 9.** FW85 modeling results.

| Object | RMSE | $R^2$ |
|---|---|---|
| $\overline{L}$ | 0.0464 | 0.9936 |
| $\overline{T_{net}}$ | 0.0204 | 0.9874 |
| $\overline{P_{in}}$ | 0.3787 | 0.9428 |

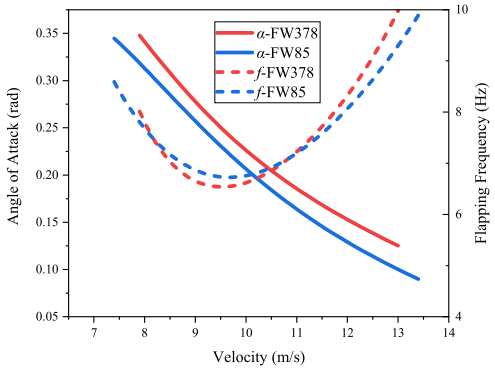


**FIGURE 11.** FW378 and FW85 steady level flight performance calculation results.

model of FW85 is established according to the method in Chapter III. The modeling result of FW85 is shown in Eq. (28) to (30). The model accuracy is shown in Table IX.

$$\left.\begin{aligned}\overline{L} &= \overline{L_0} + \overline{L_\alpha}\alpha \\ \overline{L_\alpha} &= 1.634 + 0.2855f - 0.4016V \\ &\quad - 0.02283fV + 0.08168V^2 \\ \overline{L_0} &= -0.3379 - 0.03144f + 0.1075V \\ &\quad + 0.006396fV - 0.004672V^2\end{aligned}\right\} \tag{28}$$

$$\left.\begin{aligned}\overline{T_{net}} &= \overline{T_f}f^2 - D \\ \overline{T_f} &= -0.001795 - 0.03676\alpha \\ &\quad + 0.001572V - 0.1404\alpha^2 \\ &\quad + 0.01065\alpha V - 0.00007055V^2 \\ &\quad + 0.2268\alpha^3 + 0.0004073\alpha^2 V \\ &\quad - 0.0004115\alpha V^2 \\ D &= -1.487 + 1.173\alpha + 0.3297V \\ &\quad - 2.086\alpha^2 - 0.1609\alpha V \\ &\quad - 0.0204V^2\end{aligned}\right\} \tag{29}$$

$$\left.\begin{aligned}\overline{P_{in}} &= \overline{M_{wing}}\overline{\omega} \\ \overline{M_{wing}} &= 1.194 - 0.1849f + 0.09869V \\ &\quad + 0.01688f^2 - 0.004837fV \\ &\quad - 0.002951V^2 \\ \overline{\omega} &= 1.989f(-0.00574f + 1.226)\end{aligned}\right\} \tag{30}$$

The following is a comparison between FW85 and FW378 according to the flapping wing performance calculation method in Chapter IV. As shown in Fig. 11, in the steady level flight performance, FW85 has a larger velocity envelope, and its trimmed angle of attack is lower than that of FW378, indicating that the lift characteristic of FW85 is better. There is little difference between their trimmed flapping frequencies. The calculation results show that increasing the thickness of the airfoil within a certain range can improve the steady level flight performance of the flapping wing.

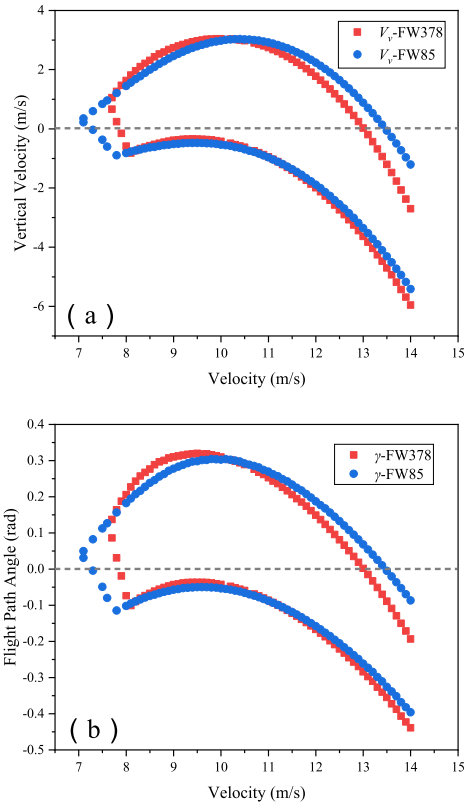


**FIGURE 12.** FW378 and FW85 steady climbing and descending trimmed state boundaries. (a) Trimmed vertical velocity boundary. (b) Trimmed flight path angle boundary.

**TABLE 10.** The maximum endurance and maximum range comparison.

| Flapping wing | $V_{E.max}$ (m/s) | $E_{max}$ (h) | $V_{R.max}$ (m/s) | $R_{max}$ (km) |
|---|---|---|---|---|
| FW378 | 9.4 | 0.69 | 10.6 | 25.01 |
| FW85 | 9.6 | 0.70 | 11.0 | 26.51 |

From the calculation results in Fig. 12, it can be seen that the difference between the steady climb and the descending flight performance of FW85 and FW378 is not large. The difference in climbing and descending performance at low speed is caused due to the better low-speed performance of FW85. The results suggest that a thicker airfoil may not further increase the cycle averaged net thrust, but it may result in additional drag.

Due to the better lift characteristics of FW85, its minimum turning radius is significantly smaller than that of FW378. However, the overload of a FMAV is usually limited by the structure. According to the maximum overload limit of 2G, it can be considered that FW85 has a slightly smaller radius than FW378 in practice as shown in Fig. 13.

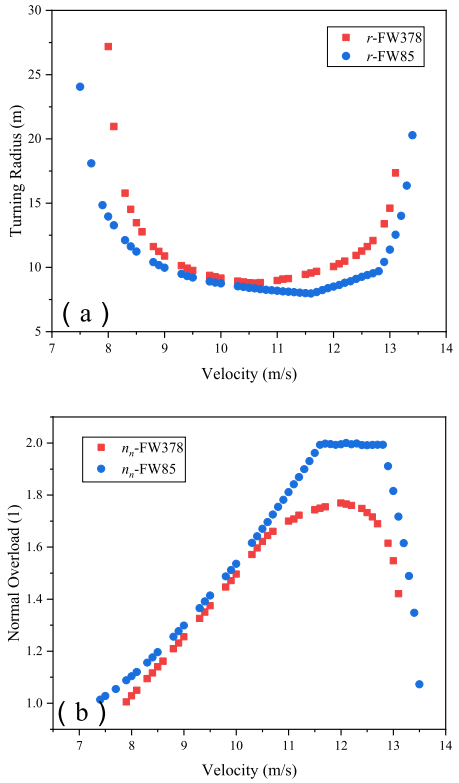


**FIGURE 13.** FW378 and FW85 steady turning trimmed state boundaries with limited overloads of 2G. (a) Trimmed turning radius boundary. (b) Trimmed normal overload boundary.

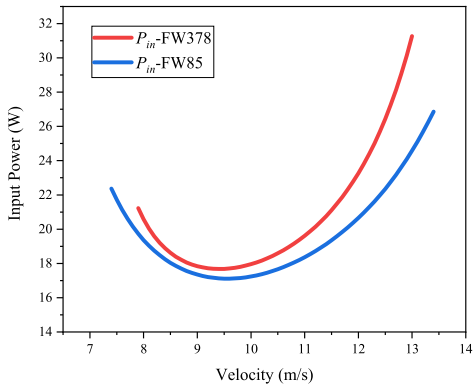


**FIGURE 14.** FW378 and FW85 power consumption performance calculation results.

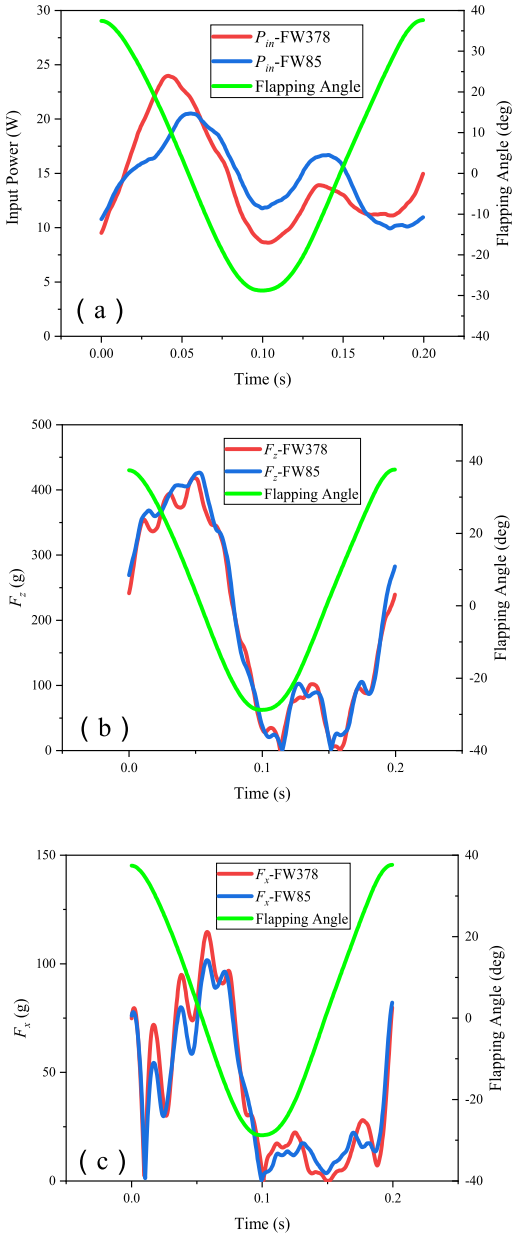


**FIGURE 15.** FW378 and FW85 instantaneous experimental data comparison (at $V = 10$m/s, $f = 5$Hz, $\alpha = 12°$ ). (a) Experimental servo motor instantaneous input power. (b) The absolute value of the z-axis force component of the load cell. (c) The absolute value of the x-axis force component of the load cell.

In terms of power consumption in the steady level flight state, it can be seen from Fig.14 that the trimmed level flight power of FW85 is smaller than that of FW378. The comparison of endurance and range of the two experimental flapping wings are in Table X. According to the comparison results, increasing the thickness of the attached airfoil within a certain range can reduce the steady level flight power and improve the endurance and range performance.

In order to study the reason why FW85 improves its power consumption characteristics compared with FW378, the instantaneous aerodynamic force and input power in the wind tunnel experimental data are extracted, as shown in Fig. 15. According to the instantaneous power curve, it can be seen that FW85 consumes less power than FW378 in the first half stage of the down stroke and the late stage of the up stroke, which shows its low power consumption characteristics at a high angle of attack. During these two periods of high angles of attack, there's little difference in the instantaneous normal force $F_z$ between the two flapping wings, so it is not the cause of the difference in power. Comparing the tangential force curve, it can be seen that FW378 has a larger tangential force in the first half stage of the down stroke. However, this difference does not directly cause the flapping shaft torque to change, but it causes an increase in the frictional force of the flapping mechanism, thus causing an increase in power

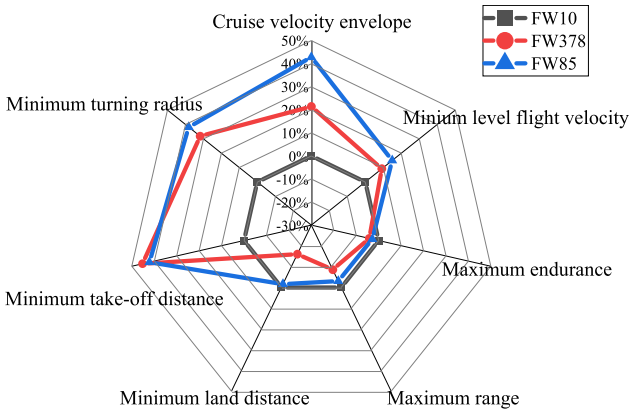


**FIGURE 16.** FW378, FW85 and FW10 flight performance comparison. (Percentage change in the performance of FW378 and FW85 is relative to FW10.)

consumption. The power consumption characteristics of the first half stage of the down stroke basically determine the power consumption characteristics of a flapping wing due to the large amplitude of power in this stage. Limited to experimental devices, the foregoing is only a preliminary analysis. The changes in the position of the pressure center will also affect the power consumption characteristics.

The performance comparison between the flapping wing with an attached airfoil to the root and the original flapping wing is shown in Fig. 16.

By comparing the flight performance of FW85 and FW378, it can be preliminarily concluded that increasing the thickness of the attached airfoil can further improve the level flight performance and reduce the endurance loss from the attached airfoil.

## VII. CONCLUSION

For the purpose of improving the performance of the flexible membrane flapping wing, a flexible flapping wing with an attached airfoil to the root is designed and tested in a wind tunnel. In order to facilitate the evaluation of the flapping wing performance, we propose to evaluate the property of the flapping wing by flight performance rather than aerodynamic performance. At the same time, a set of methods is proposed to establish the flapping wing mathematical model based on wind tunnel experimental data. The model has high precision and can meet the requirements of the flapping wing performance evaluation. Since the model is in a continuous polynomial form, it has a limitted extrapolation ability in the linear range, which can support the calculation of the performance in the untested state. After comparing the performance of the Dove's flapping wing and the experimental flapping wing with the complete EPPLER 378 airfoil attached to Dove's flapping wing root, the following conclusions are obtained:

a. By attaching an airfoil with certain thickness to the root, partial airflow separation is suppressed. The level flight velocity envelope is expanded, especially with a small level flight velocity, which has great benefits to the control characteristics of the landing phase.
b. The flapping wing with a complete airfoil attached to the root causes an increase in the flapping shaft torque, due to the increase of the instantaneous aerodynamic force. The increase in the flapping shaft torque results in a slight increase in power consumption compared with the original flapping wing during the entire trimmed states. Besides, there is a small decrease in endurance and range.
c. The attachment of a complete airfoil to the root reduces the drag caused by airflow separation, thereby increasing the net thrust of the flapping wing, which greatly increases the climbing capacity and effectively reduces the requirements for the takeoff site.
d. The flapping wing with a complete airfoil attached to the root increases the cycle-averaged lift, resulting in a significant reduction in the radius of steady turning and improving maneuverability.

In addition, in order to study the performance difference of flexible flapping wings with airfoils of different thickness attached near to the root, the EJ 85 airfoil with a similar shape and camber to the EPPLER 378 but larger thickness is attached to the original flapping wing root. The same wind tunnel experiment is carried out to establish the mathematical model of the flapping wing with EJ 85 airfoil attached. By comparing the performance of the flapping wing with EPPLER 378 airfoil and that with EJ 85 airfoil, the following conclusions are obtained:

a. Increasing the thickness of the attached airfoil within a certain range can further expand the speed envelope of the flapping wing and reduce the minimum level flight velocity.
b. Increasing the thickness of the attached airfoil may not further improve the climbing performance and turning performance of the flapping wing.
c. By properly selecting the thickness of the attached airfoil, the increase in the level flight power after the airfoil attached can be reduced.

## ACKNOWLEDGMENT

The authors gratefully acknowledge the special OriginPro Learning Edition for students from OriginLab for the support of this work.

## REFERENCES

[1] A. E. Holness, H. A. Bruck, and S. K. Gupta, "Characterizing and modeling the enhancement of lift and payload capacity resulting from thrust augmentation in a propeller-assisted flapping wing air vehicle," *Int. J. Micro Air Vehicles*, vol. 10, no. 1, pp. 50–69, Mar. 2018.
[2] M. Karásek, F. T. Muijres, C. De Wagter, B. D. W. Remes, and G. C. H. E. de Croon, "A tailless aerial robotic flapper reveals that flies use torque coupling in rapid banked turns," *Science*, vol. 361, no. 6407, pp. 1089–1094, Sep. 2018.
[3] M. Keennon and J. Grasmeyer, "Development of two MAVs and vision of the future of MAV design," in *Proc. AIAA Int. Air Space Symp. Expo., Next 100 Years*, Dayton, OH, USA, 2003, p. 2901.
[4] J. Gerdes *et al.*, "Robo Raven: A flapping-wing air vehicle with highly compliant and independently controlled wings," *Soft Robot.*, vol. 1, no. 4, pp. 275–288, Dec. 2014.

[5] M. Keennon, K. Klingebiel, and H. Won, "Development of the nano hummingbird: A tailless flapping wing micro air vehicle," in *Proc. 50th AIAA Aerosp. Sci. Meeting Including New Horizons Forum Aerosp. Expo.*, Nashville, TN, USA, 2012, p. 588.
[6] W. Send, M. Fischer, K. Jebens, R. Mugrauer, A. Nagarathinam, and F. Scharstein, "Artificial hinged-wing bird with active torsion and partially linear kinematics," in *Proc. 28th Congr. Int. Council Aeronautical Sci.*, Brisbane, QLD, Australia, 2012, pp. 1–10.
[7] D. Mueller, J. W. Gerdes, and S. K. Gupta, "Incorporation of passive wing folding in flapping wing miniature air vehicles," in *Proc. Int. Design Eng. Tech. Conf. Comput. Inf. Eng. Conf.*, San Diego, CA, USA, 2009, pp. 797–805.
[8] J. Calogero, M. Frecker, Z. Hasnain, and J. E. Hubbard, Jr., "Optimization of spatially distributed contact-aided compliant mechanisms in a dynamic structure," in *Proc. Conf. Smart Mater., Adapt. Struct. Intell. Syst.*, Snowbird, UT, USA, 2017, p. V001T06A010.
[9] D.-K. Kim and J.-H. Han, "Smart flapping wing using macrofiber composite actuators," *Proc. SPIE*, vol. 6173, Apr. 2006, Art. no. 61730F.
[10] Z. Li, S. Suntharasantic, S. Bai, and P. Chirarattananon, "Aeromechanic models for flapping-wing robots with passive hinges in the presence of frontal winds," *IEEE Access*, vol. 6, pp. 53890–53906, 2018.
[11] E. C. Stewart, M. Patil, R. A. Canfield, and R. D. Snyder "Aeroelastic shape optimization of a flapping wing," in *Proc. 10th AIAA Multidisciplinary Design Optim. Conf.*, Boston, MA, USA, 2014, pp. 57–60.
[12] W. Yang, L. Wang, and B. Song, "Dove: A biomimetic flapping-wing micro air vehicle," *Int. J. Micro Air Vehicles*, vol. 10, no. 1, pp. 70–84, Mar. 2018.
[13] S. Widhiarini *et al.*, "Bird-mimetic wing system of flapping-wing micro air vehicle with autonomous flight control capability," *J. Bionic Eng.*, vol. 13, no. 3, pp. 458–467, Jul. 2016.
[14] M. K. Heerenbrink, L. C. Johansson, and A. Hedenström, "Power of the wingbeat: Modelling the effects of flapping wings in vertebrate flight," *Proc. Roy. Soc. A, Math., Phys. Eng. Sci.*, vol. 471, no. 2177, Apr. 2015, Art. no. 20140952.
[15] F. Peng *et al.*, "An experimental research about the characteristics of thrust and power of FMAV," *J. Northwestern Polytech. Univ.*, vol. 34, no. 6, pp. 976–981, Dec. 2016.
[16] W. Yang, B. Song, and G. Gao, "Flight performance estimation of bionic flapping-wing micro air vehicle," *J. Northwestern Polytech. Univ.*, vol. 36, no. 4, pp. 636–643, Aug. 2018.
[17] J. Xuan, Z. Yang, P. Nian, and D. Ma, "Calculation methods of flight performance of flapping wing aircrafts based on energy theory and slipstream theory (September 2018)," *IEEE Access*, vol. 6, pp. 68176–68183, 2018.
[18] M. Sun, J. Wang, and Y. Xiong, "Dynamic flight stability of hovering insects," *Acta Mechanica Sinica*, vol. 23, no. 3, pp. 231–246, Jun. 2007.
[19] B. N. Pamadi, *Performance, Stability, Dynamics, and Control of Airplanes*. Hampton, VA, USA: American Institute of Aeronautics and Astronautics, 2004, pp. 70–73.
[20] K. Liu, A. Da Ronch, D. Li, and J. Xiang, "Modeling of unsteady aerodynamics for a flapping wing," *IFAC-PapersOnLine*, vol. 48, no. 28, pp. 404–408, Oct. 2015.
[21] J.-S. Lee and J.-H. Han, "Experimental study on the flight dynamics of a bioinspired ornithopter: Free flight testing and wind tunnel testing," *Smart Mater. Struct.*, vol. 21, no. 9, Sep. 2012, Art. no. 094023.

**PENG NIAN** was born in Jingtai, Gansu, China, in 1992. He received the B.E. degree in flight vehicle design and engineering from Northwestern Polytechnical University, Xi'an, where he is currently pursuing the Ph.D. degree in flight vehicle design.

He has authored three articles and more than five inventions. His research interests include ornithopter design, dynamic simulation of ornithopter, amplitude-variable flapping mechanism design, and free-flight test of ornithopter.

**BIFENG SONG** was born in Fengxiang, Shaanxi, China, in 1963. He received the B.E., M.S., and Ph.D. degrees in aircraft design engineering from Northwestern Polytechnical University, China, in 1985, 1988, and 1998, respectively.

From 1991 to 1993, he was an Assistant Professor. From 1993 to 1998, he was an Associate Professor. Since 1999, he has been a Professor with the School of Aeronautics, Northwestern Polytechniacal University, China. His research interests include the aircraft design, aircraft structure design, multidisciplinary design optimization, high survivability technology and reliability, and bionic MAV.

**JIANLIN XUAN** received the B.E. and master's degrees in aircraft design engineering from Northwestern Polytechnical University, Xi'an, China, in 2004 and 2007, respectively, where he is currently pursuing the Ph.D. degree in flight vehicle design.

He has been teaching with the School of Aeronautics, Northwestern Polytechnical University, since 2007. His current research interests include the control of flight vehicle system and its application in the industrial process, the influence for flight vehicle from complex environment, the load simulation for flight vehicle, and energy saving control in flight systems.

**WENQING YANG** was born in Yangquan, Shanxi, China, in 1980. She received the B.E., M.S., and Ph.D. degrees in aircraft design engineering from Northwestern Polytechnical University, China, in 2004, 2007, and 2010, respectively.

From 2010 to 2012, she held a postdoctoral position. From 2013 to 2015, she was an Assistant Professor. Since 2015, she has been an Associate Professor with the School of Aeronautics, Northwestern Polytechniacal University, China. Her research interests include bionic MAV, flapping-wing, aerodynamic performance and design of MAV, CFD, and wind tunnel experimental research.

**YUANBO DONG** was born in Luoyang, Henan, China, in 1994. He received the B.E. degree in mechanics from Zhengzhou University, in 2017, and the Ph.D. degree in aircraft design from Northwestern Polytechnic University. His current research interests include the aerodynamic mechanism of flapping wing and aerodynamic design of micro flapping wing aircraft.